ARTICLE

A Motion-Stabilized W-Band Radar for Shipboard Observations of Marine Boundary-Layer Clouds

**Ken Moran · Sergio Pezoa · Chris Fairall ·
Chris Williams · Tom Ayers · Alan Brewer ·
Simon P. de Szoeke · Virendra Ghate**

Abstract   Cloud radars at X, Ka and W-bands have been used in the past for ocean stud-
ies of clouds, but the lack of suitable stabilization has limited their usefulness in obtaining
accurate measurements of the velocity structure of cloud particles and the heights of cloud
features. A 94 GHz (W-band) radar suitable for use on shipboard studies of clouds has been
developed that is small and lightweight and can maintain the radar's beam pointing in the
vertical to reduce the affects of the pitch and roll of the ship. A vertical velocity sensor on the
platform allows the effects of the ship's heave to be removed from the measured cloud particle
motions. Results from the VAMOS Ocean-Cloud-Atmosphere-Land Study Regional Exper-
iment (VOCALS-Rex) field program on the NOAA vessel *Ronald H. Brown* demonstrate
the improvements to the cloud measurements after the ship's motion effects are removed.
The compact design of the radar also makes it suitable for use in aircraft studies. The radar
is being repackaged to fit in an aft bay of a NOAA P3 aircraft to observe sea-spray profiles
during ocean storms.

Keywords   Cloud radar · Marine boundary-layer clouds · Shipboard motion stabilization ·
VOCALS 2008

K. Moran (✉) · C. Williams
Cooperative Institute for Research in the Environmental Sciences, University of Colorado,
Boulder, CO, USA
e-mail: ken.moran@noaa.gov

S. Pezoa · C. Fairall · T. Ayers
NOAA Earth System Research Laboratory/PSD, Boulder, CO, USA

A. Brewer
NOAA Earth System Research Laboratory/CSD, Boulder, CO, USA

S. P. de Szoeke
Oregon State University, Corvallis, OR, USA

V. Ghate
Rutgers University, New Brunswick, NJ, USA

🖄 Springer

1 Introduction

The dynamics and microphysical properties of cloud droplets within marine boundary-layer stratocumulus clouds are basic to understanding the role clouds play in air-sea interaction and their influence on radiative processes (Stephens et al. 1990). Shipboard cloud studies over the ocean off the coast of western Chile have taken place during the last decade to better characterize the dynamics of marine boundary-layer clouds and to provide new datasets that can lead to improved modelling of the radiative process (Bretherton et al. 2004). Millimetre wavelength cloud radars in the Ka-band (35 GHz) and the W-band (94 GHz) have historically been used to measure the velocity structure and distribution of small cloud particles from non-precipitating and weakly precipitating (drizzle) clouds (Frisch et al. 1995; Vali et al. 1998; Kollias and Albrecht 2000). Ka-band radars have played an important role in measuring cloud properties from land-based sites, where the radar's physical properties such as size and weight are not a factor in the design (Ackerman and Stokes 2003).

For mobile platforms such as ships and aircraft, the requirements for carefully engineered packaging as well as motion-compensation place a demand on the size and weight of the radar (Pazmany et al. 1994; Li et al. 2004). To provide the sensitivity needed for land-based cloud observing sites, Ka-band radars used at field sites are typically characterized by large antenna diameters (2–4 m) and integration times of several seconds. The smaller size and reduced weight of W-band cloud radars make them better suited for shipboard as well as aircraft deployments. The wavelength (λ) dependence $\left(\lambda^{-4}\right)$ of the radar cross-section offers a factor of 50 advantage in sensitivity to a W-band radar over a similar Ka-band design. This advantage can be used to provide a performance suitable to mobile platforms without sacrificing the sensitivity of the radar. Smaller antennae at the W-band with less mass make the task of beam steering more manageable. For mobile platforms short dwell times are often used (<1 s) to reduce the effects of platform motion. Independent measurements of the platform motion using external velocity sensors can be used to remove motion-caused biases.

W-band radars became a tool for studying the small water droplets in clouds after the pioneering work of Lhermitte (1987, 1988, 1990). The application to cloud studies followed this work and radar systems used by research groups greatly expanded in the period 1990–2000. Along with numerous Ka-band radars the community of cloud researchers used the two wavelengths to study cloud microphysics to provide a greater understanding of their capabilities and limitations (Sekelsky and McIntosh 1996; Sekelsky et al. 1999; Kollias et al. 2007).

The Atmospheric Radiation Measurement (ARM) program sponsored by the U.S. Department of Energy, fielded several Ka-band millimetre wavelength cloud-profiling radars (MMCR) starting in 1996 (Ackerman and Stokes 2003). These radars pointed vertically, ran continuously and unattended and provided a record of cloud-particle dynamics derived from the Doppler spectrum of the backscattered signal (Moran et al. 1998). The radars were the cornerstone instruments designed to characterize the macrophysical cloud properties as well as to observe the dynamics of particle behaviour in order to improve understanding of the evolutionary processes that take place in continental clouds.

Ground-based radars are capable of resolving the vertical distribution of cloud layers and can produce statistical properties of cloud boundaries and radar reflectivities (Dong et al. 2005).The kinematic structure within stratus clouds has been used in studies of turbulence intensity, entrainment and updraft and downdraft structures (Kollias and Albrecht 2000; Damiani et al. 2006). Techniques have also been developed for retrieving the cloud, ice crystal and drizzle particle size distributions (Gossard 1988, 1994; Frisch et al. 1995; Mace et al. 2002).

NOAA's Environmental Technology Laboratory developed its own version of the ARM MMCR and participated in the Surface Heat budget of the Arctic Ocean (SHEBA) field program in 1997–1998. NOAA's radar later participated in several cruises aboard the NOAA vessel *Ronald H. Brown*, for field experiments in 1999, 2001 and 2003 that investigated the structure of marine stratus clouds and evaluated the cloud properties derived from radar measurements (Webster et al. 2002; Bretherton et al. 2004; Kollias et al. 2004). While the NOAA radar measured non-precipitating cloud types with excellent sensitivity and temporal and spatial resolution, the ship's motion caused problems when measuring the cloud particle dynamics. The pitch and roll of the ship caused the fixed radar beam to wander off vertical and the natural horizontal winds combined with the ship's forward and vertical motion induced errors and artifacts into the particle velocities. The radar's 2-m antenna had a fixed mount and the cumbersome radio frequency (RF) electronics were mounted inside the operating container making it difficult to configure the radar for any type of motion compensation hardware. At one point, the entire sea container that is used to house the radar was under consideration to be tilted fore and aft and side-to-side with hydraulic risers to maintain the radar beam vertical. This proved too challenging an undertaking.

Observations of marine boundary-layer clouds have taken place since the mid 1990s using W-band radars mounted in aircraft (Pazmany et al. 1994; Vali et al. 1995) and have provided details of the internal structure of marine stratus clouds (Vali et al. 1998). While the airborne platforms provide measurements during short flight intervals a continuous record of the properties of marine boundary-layer clouds could be provided by a shipboard radar if the velocity measurements were corrected for the ship's motion. There was a growing need for the development of a radar that could be easily configured for shipboard use that included motion compensation hardware and velocity correction techniques. A radar with the ability to provide an extended time series of the structure of maritime clouds can help in understanding the evolutionary processes at work (Kollias et al. 2007).

In this paper we describe a new seagoing W-band radar including design characteristics, sensitivity and calibration issues, motion stabilization and correction, and give some examples of marine boundary-layer cloud studies from the first field deployment. Plans for future work and a summary conclude the paper.

2 Radar Design

Because radar parameters tend to span many orders of magnitude, it is traditional to use logarithmic terminology to characterize many variables. The term dB (decibel) is a generic designation of the ratio of two values (say X_2 and X_1), such that $dB = 10 \log_{10}(X_2/X_1)$ (Benedict 1967). Other terminology includes dBm, which defines the ratio of power to an absolute power. We also define $dBZ = 10 \log_{10}(Z)$ where Z is the 'reflectivity factor' (sixth moment of the size distribution of scatterers—Lhermitte 2002).

2.1 Characteristics

The requirements of a cloud-profiling radar designed for observing maritime boundary-layer clouds aboard ship should have sufficient sensitivity to make observation of pre-drizzle conditions in clouds with reflectivity of about -30 dBZ to an altitude of 3 km. A modular design will allow for the RF section to be separated from the other electronics and mounted in a frame attached to a stabilized beam steering unit to compensate for the ship's pitch and roll.

The archiving of the full Doppler velocity spectrum of the echo from each range will allow complex distributions of particle sizes and fall speeds to be evaluated from the recorded spectra. The radar platform's vertical velocity due to the ship's heave will need to be measured and removed from the particle's speed. A spatial and temporal resolution of 25 m and 0.3 s will provide a detail look at the cloud structure on a scale that will show the evolution of cloud development.

Beginning in 2006 NOAA's Physical Science Division of the Earth Systems Research Laboratory designed and developed a W-band radar suitable for studying marine stratocumulus clouds from research vessels such as NOAA's *Ronald H. Brown*. The radar was completed in time to be part of the VAMOS Ocean-Cloud-Atmosphere-Land Study Regional Experiment (VOCALS-Rex) in October to November 2008 (Woods et al. 2011). The radar is housed in a modified sea container that is routinely used on cruises. A rooftop hatch allows for the installation of an antenna port with a shroud and a low loss radome for weather protection. The radar has a split design that allows the electronics to be in two separate packages: (1) a small light-weight section that contains all the RF electronics including the transmitter, antenna, receiver and waveguide, and (2) an electronics rack that houses the computers, intermediate frequency (IF) electronics and transmitter power source. The small RF section was designed to weigh less than 50 kg and have a centre of gravity near the geometric centre of its support frame, 0.6 m × 0.6 m × 1.0 m. These mechanical features provided suitable characteristics to design and build a small autonomous positioner that would compensate for the pitch and roll of the ship and keep the radar beam pointed vertically during the cruise. The 0.3-m diameter antenna and the 1.7 kW peak power transmitter provide a sensitivity of −33 dBZ at 2 km, sufficient to detect non precipitating marine stratocumulus boundary-layer clouds at an altitude of 3 km. The time interval between successive beams is typically 0.3 s to provide sufficient temporal resolution needed to accurately resolve the effects of the vertical motion of the ship.

Our design for a stabilized platform requires the radar to have a lightweight RF section that contains the antenna, transmitter and waveguide components that can be easily steered by a motion stabilizer (Fig. 1). The stabilizer is in the form of a cradle with two orthogonal rocking axes that can easily swing back and forth and side to side to compensate for the pitch and roll of the ship. The entire RF section and antenna is housed in an open frame for easy access and is balanced near the geometric centre of the frame. The light weight and small size allowed for a robust design of the control system for the stabilizer that works independently of the radar with its own PC based proportional-integral-derivative (PID) controller.

A Kongsberg ship motion sensor measures the radar platform's pitch and roll as well as the platform's vertical velocity and provides outputs to the stabilization controller as well as for archiving. The roof of the container that houses the radar has a 1.3 m × 1.3 m removable plate with a 1.0-m diameter hole for a rolled edge cylindrical shroud with a slanted radome cover. The cover is made of shrink wrap material identical to that used to weatherize boats and marine gear and provides a low loss window through which the radar beam passes. A coherent up/down converter can provide narrow output pulses of 100 ns and receiver bandwidths to 10 MHz for range resolution down to 15 m. Signal processing software in the digital receiver computes a fast Fourier transform (FFT) of the Doppler power spectrum for each sampled range and the first three moments are estimated using conventional methods (Kollias et al. 2007). Hourly spectra and moments files are saved (in netCDF) to an external spectra disk at the rate of about 20 Gbytes per day. Mean power estimates are converted to reflectivity through calibration software and moment files are archived hourly. Details of the radar and the current calibration scheme are contained in Appendix A.

Fig. 1 Photo of the stabilized
platform with the radar frame
resting in the cradle. The roof
hatch with the slanted radome is
located above the cylindrical
antenna shroud

2.2 Sensitivity

For cloud studies in the marine boundary layer measurements should be sensitive to non-precipitating weak stratocumulus clouds with reflectivities in the range of -30 dBZ with heights up to several kilometres. An estimate of the radar's ability to detect weak clouds can be made by computing the minimum reflectivity as a function of height using the radar's characteristics and operational constants such as waveguide losses, antenna characteristics and transmitted power (Table 1 lists the characteristics of the NOAA W-band radar during the VOCALS cruise and Table 2 lists the operating constants for the cruise.)

To estimate the sensitivity at a particular range the radar reflectivity comes from an estimate of the minimum detectable signal (MDS):

$$dBZ = MDS + 20 \log (R) + RC \tag{1}$$

where *MDS* is the estimated minimum detectable signal in decibels above a milliwatt (dBm), *R* is the range in metres and the radar constant (*RC*) is in dB (for simplicity we have removed the physical units). The radar constant is derived from the Probert-Jones (1962) radar equation and takes the form:

$$RC = 10 \log_{10} \left(\frac{512 \ln(2) \lambda^2 10^{18} L_{SYS}}{P_T G^2 \theta \phi \Delta R \pi^3 K^2} \right) \tag{2}$$

Using the values from Table 2 the radar constant during the VOCALS cruise was $RC = 19.6$ dB. The estimate of the minimum detectable signal is obtained from the radar operating temperature, receiver bandwidth and the threshold for signal detection:

Table 1 Characteristics of NOAA's W-band radar during VOCALS (col. 2), proposed P3 aircraft sea-spray study (col. 3) and ARM's MMCR (col. 4)

Platform	Shipboard (VOCALS cruise)	NOAA P3 aircraft (planned)	Land based ARM MMCR
Application	Cloud properties	Sea spray	Cloud properties
Frequency (GHz)	94.56	94.56	34.86
Peak/avg. power (Watts)	1,750/3	1,750/1	200/0.3
Platform altitude	Sea surface	1.5–3 km	Earth surface
PRF_{MAX} (KHz)	8.33	10	11.1
Antenna	Cassegrain	Cassegrain	Cassegrain
Diameter (m)	0.3	0.5	2.0
Ant. gain dB/beamwidth	46/0.7°	48/0.5°	53/0.3°
Antenna beam positioner	Pitch–Roll compensation	None	None
Pointing directions	Vertical	Nadir	Vertical
Polarization	No	No	No
Pulse integration	No	No	6
Pulse width (ns)	167	125	292
Cell size (m)	25	18.75	44
Number of ranges	120	100–200	139
Maximum range (km)	3	2.25	6.1
Velocity resolution (m s^{-1})	0.103	0.062	0.045
Max radial velocity (m s^{-1})	±6.6	±7.9	±5.7
Temp. stabilized RF	No	Yes	No
Pressurized enclosure	No	Yes	No
Spectral processing/time between beams (s)	128 pt FFT 8 averages ≈0.3	256 pt FFT 8 averages ≈0.2	256 pt FFT 20 averages ≈1.5
Data formats	netCDF, Ascii	netCDF, Ascii	netCDF
Estimated sensitivity (dBZ) $R = 2$ km (no atmos losses)	−33	−33	−37

$$MDS = kT_{OP}B_{NE}SNR_{Min}10^3 \qquad (3)$$

where λ is the radar wavelength (m), L_{SYS} is the system losses including matched filter loss (see Doviak and Zrnic 1993), P_T is the peak transmitted power (milliwatts), G is the antenna one way gain—includes radome loss, ϕ = beamwidth (radians), θ = beamwidth (radians), ΔR = range cell depth (m), K is the complex index of refraction for water, k is the Boltzman's constant, T_{OP} is the radar receiver's operating temperature in K, B_{NE} is the noise equivalent bandwidth of the of the receiver in Hz, SNR_{min} is the threshold of signal-to-noise ratio for detectable signals and MDS is in units of milliwatts.

The radar operating temperature can be computed from the receiver noise figure, F_n, with $T_{OP} = 290F_n$. The noise equivalent bandwidth, B_{NE}, is related to the characteristics of the receiver bandwidth filter and the number of transmitted pulses that are coherently integrated

Table 2 System constants for the W-band radar during VOCALS

λ = wavelength mm	3.17
L_{TX} = transmit path loss (dB)	4.0
L_{RX} = receiver path loss (dB)	2.2
L_{MF} = matched filter loss (dB)	2.3
P_T = Peak transmitted power (dBm)	62.4
G = Antenna one way gain—includes radome loss (dB)	45.9
$\theta - \phi$ beamwidths (°)	0.76, 0.70
Antenna near field distance $\left(2D^2/\lambda\right)$ (m)	65
ΔR range cell height (m)	25
$|K|$ – complex index of refraction of water	0.712 @ 0°C
	0.779 @ 10°C
	0.828 @ 20°C
Receiver noise figure dB/T_{OP} (K)	5.0/917
Noise equivalent bandwidth (MHz)	6.24
Processed signal gain, G_{RP} (dB)	185.2

(*NCI*) by the signal processor: $B = B_{NE}/NCI$. The W-band radar does not use coherent pulse integration and therefore $NCI = 1$.

There are several techniques to estimate the threshold of signal (cloud) detection using the signal-to-noise ratio, *SNR*, of the observed spectrum. A *SNR*$_{min}$ can be measured from a threshold of detected cloud data or by using an estimate from the *SNR* receiver statistics. In earlier work that determined the *SNR* threshold to distinguish significant echoes in the Doppler power spectrum, Riddle et al. (1989) provided an empirical relationship by observing clear-air returns from a 50 MHz wind profiler:

$$SNR_{\text{threshold}} = \frac{25\sqrt{N_F - 2.3125 + \frac{170}{N_P}}}{N_F N_P} \tag{4}$$

where N_F is the number of FFTs averaged to form the power spectrum and N_P is the number of points in the FFT. While this threshold was meant to provide for a robust signal threshold, rather than a minimum detectable signal level, it was used for many years as a reasonable estimate. Using the values during VOCALS, this $SNR_{\text{threshold}} = -11.9$ dB.

We can also estimate the minimum *SNR* from the statistical properties of a Doppler power spectrum (see Appendix B). From this estimate SNR_{Min} can be written in terms of the N_P and N_F, similar to Riddle et al. (1989).

$$SNR_{Min} = \frac{a}{N_P\sqrt{N_F}} \tag{5}$$

where a is a threshold factor for the signal to be greater than the standard deviation of the spectral noise. Here the VOCALS parameters yield a *SNR* threshold of -21.7 dB

To evaluate the threshold for VOCALS data we found a clear-sky period and assessed the histogram of the *SNR*, which will provide a noise-only estimate of the receiver's characteristics. The mean noise-only estimate of *SNR* is -20.3 dB and two standard deviations away the threshold is -17.9 dB (here there was minimal influence from false detections due to receiver noise). Comparing this threshold with the other estimates, the threshold value of

Table 3 SNR threshold estimates from empirical methods (Riddle), spectral probability statistics (Appendix B) and *SNR* measurements

SNR threshold estimates	Threshold (dB)	Threshold factor a
Empirical methods	−11.9	23.38
Probability statistics	−21.7	2.45
SNR measurements	−17.9	5.87
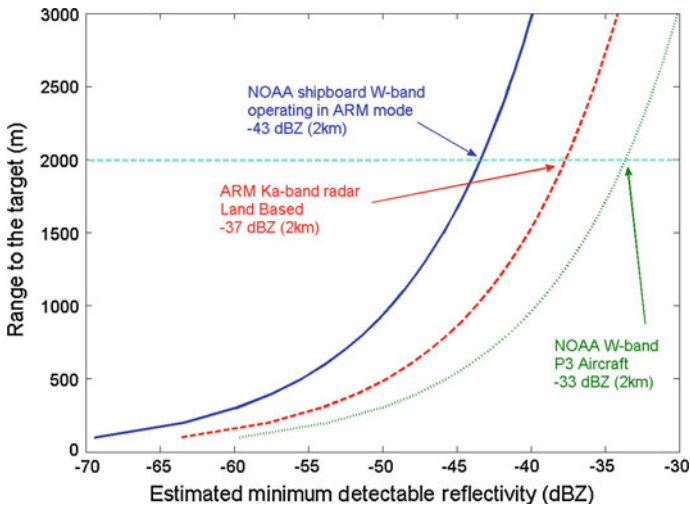
Fig. 2 Profile of radar sensitivity in dBZ for the W-band radar operating in the ARM mode (*blue solid*), airborne W-band (*green dots*) and land based ARM Ka-band cloud radar (*red dash*). The sensitivity profile for VOCALS is identical to the curve for the airborne radar (*green dots*)

−21.7 dB from Appendix B appears too sensitive and will produce a significant number of false cloud-boundary detections. The Riddle estimate appears not sensitive enough in this case and will miss detections of a significant number of cloud boundaries. Our noise-only threshold is 6.0 dB more sensitive than the Riddle estimate of −11.9 dB. Using Eq. 5, we can compute the value of the threshold factor, 'a', for these three threshold estimates, where $N_P = 128$ and $N_F = 8$ (Table 3).

Using our *SNR* threshold of −17.9 dB from clear-sky conditions, the minimum detectable reflectivity Z_{min} (2 km) is −33 dBZ, as shown in Table 1, column 2. We can compare the sensitivity of the ARM MMCR to the NOAA W-band radar if we use the simulated operating characteristics of the W-band that match those of the ARM radar (Moran et al. 1998). The ARM's MMCR has 7 dB more antenna gain while using lower loss waveguide components (+2 dB) and processes more pulses (+3 dB). These operating advantages of the Ka-band radar are offset by the 17 dB radar cross-section advantage of operating at a shorter wavelength for the W-band. The curves in Fig. 2 show the computed sensitivity profiles with height for three radar configurations. The curves' shapes follow the range-squared dependence for reflectivity. For the VOCALS cruise the green curve in Fig. 2 is used since it has the same sensitivity as for planned aircraft flights. Here the reflectivity estimates range from better than −50 dBZ at a few hundred metres from the surface to about −29 dBZ at 3 km providing sufficient sensitivity to detect most marine stratocumulus clouds.

3 Motion Stabilized Platform

Fixed beam radars aboard a ship at sea will have the ship's motion embedded in the cloud-droplet velocity profiles measured by the radar. The roll and pitch motions of the ship tilt the beam from vertical so that horizontal motions, either atmospheric or due to the ship's forward speed, have a component along the radial beam direction producing a fluctuating offset in the velocities. The vertical motion of the radar platform due to the heave of the ship adds artifacts to the particles' motions, even with a stabilized beam.

During light sea conditions where pitch and roll are limited to less than $\pm 5°$ over 5 s, the speed of the ship and the prevailing winds broaden the velocity spectrum and induces a radial component of the horizontal wind into the particle motion. A $10\,\mathrm{m\,s^{-1}}$ wind and a $3°$ tilt into the wind appears as a $0.52\,\mathrm{m\,s^{-1}}$ bias in the vertical wind, where a $0.5°$ tilt results in a bias of about $0.09\,\mathrm{m\,s^{-1}}$. A small overall tilt results in manageable biases in the velocity profiles. A vertical motion sensor can provide error corrections to the measured radar velocity profile, when the beam's direction can be maintained at or near vertical.

The NOAA W-band radar's electronics and antenna are housed in a small stabilized platform that can compensate for the ship's pitch and roll using two independent axes. The Kongsberg sensor, which provides the pitch and roll measurements used by the stabilization controller, also provides a measure of the radar's instantaneous vertical velocity that can be used to correct for the ship's heave.

A view of the stabilized platform with the radar electronics frame installed is shown in Fig. 1. The platform is elevated and is mounted on a rigid stand attached to the floor of the container. Two DC servo motors with gear reducers provide the two-axis motion that compensates for pitch and roll. A small plastic cylinder that houses the antenna is shown in the figure and is lined with microwave absorber to act as a safety shield. The roof top hatch has a 1-m diameter cylindrical extension with a slanted top and is covered with a low loss shrink wrap plastic that acts as the radome cover for the antenna. The opening is sufficient to allow for greater than $\pm 10°$ tilt of the antenna. Moderate to heavy seas with pitch and roll greater than $10°$ are considered very active and create problems in accurate operation of the stabilizer.

Attached to the base of the motion-stabilized platform is the Kongsberg Motion Reference Unit (MRU-Z) with a two-axis rotational position/rate sensors and a separate heave sensor. The sensor is a three-axis solid state optical gyroscope that provides pitch and roll measurements to better than $0.15°$ dynamic accuracy at an output rate of 100 Hz. A block diagram of the motion stabilizer (Fig. 3) shows the components for one axis of the two-axis controllers (roll and pitch axis controllers are identical). The motion controller computes an error signal, $e(t)$, that provides the correction signal to the driver amplifier for the motors in each individual axis. The feedback controller provides servo motor correction signals used to compute speed and brake control while the gear reduction unit drives the axle. Mechanical tilt-limit switches for each axis are used as inputs to the brake control software and disable the drive signals if the limits are reached. The Kongsberg MRU-Z sensor provides analog outputs for use in the two-axis motion controllers as well as digital outputs used to archive the platform's pitch, roll and heave measurements. The Crossbow sensor attached to the elevated stand provides digital data for the pitch and roll of the ship (archived for reference).

A control algorithm maintains vertical by comparing the measured roll or pitch position with the command position (pitch = 0, roll = 0). The mechanical offset between the gravity vector and the vertical beam is typically less than $0.2°$. The PID controller is used in a standard configuration to provide smooth control with minimal vertical offset, limited overshoot and fast response time. The motion control is adjusted through the gain setting for each function:
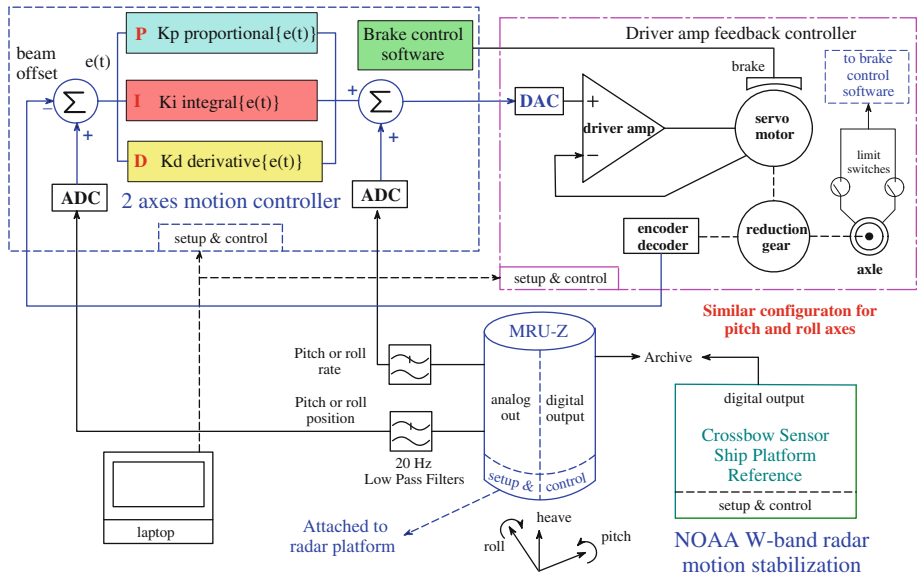
Fig. 3 Block diagram of the stabilized platform control system: two-axis motion controller, driver amplifier with feedback control, servo motors with reduction gear, MRU-Z and Crossbow motion sensors

K_p, K_i, and K_d. *Proportional* control improves response time, *integral* control eliminates steady-state errors and *derivative* control improves overshoot. During the initial sea trials on the VOCALS cruise the control parameters were adjusted until satisfactory response was achieved for the varying sea conditions. Adjustment of the control parameters is required if the sea conditions change significantly.

4 Field Test During VOCALS

4.1 Stabilized Platform Operations

In the autumn of 2008 PSD's new W-band radar was used in the VOCALS field experiment that was conducted off the west coast of Chile to provide observations of the marine cloud environment aboard the NOAA vessel *Ronald H. Brown*. The cruise had two separate legs with a stop in Arica, Chile at mid point. On the first leg of the cruise the radar experienced a problem that caused some of the transmit pulse to leak into the receiver. This damaged the low noise amplifier (LNA) resulting in significant loss of sensitivity. During the layover in Arica the problem was corrected and the second leg of the cruise provided the first reliable measurements of marine cloud structures from a stabilized radar. Preliminary scientific results from the cruise that demonstrate the systems capabilities were presented at ISARS 2010 (Fairall et al. 2010).

The objective of stabilizing the beam is to maintain minimal mean beam tilt while providing small standard deviation in the platform's roll and pitch. The vertical position of the platform sensor is zeroed with respect to the levelled antenna during calibration thus eliminating any offset between the measured vertical gravitational vector of the Kongsberg and
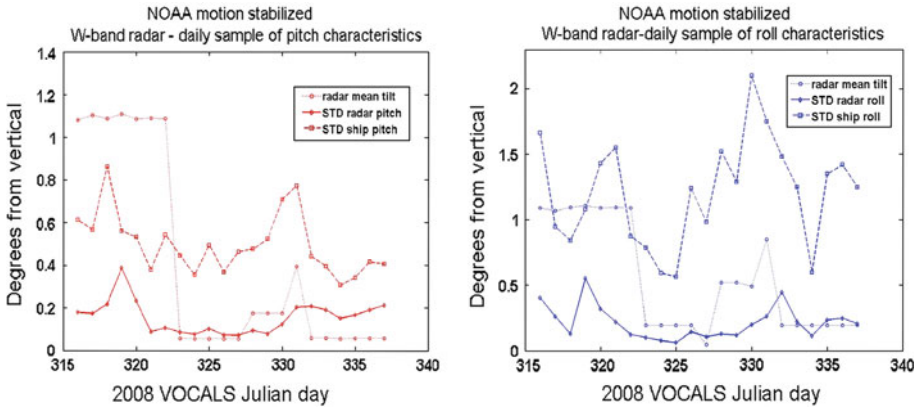
Fig. 4 Mean tilt (*dots-circles*), STD ship (*dashes-squares*), STD radar (*solid-triangles*), from the daily samples of pitch (*left panel*) and roll (*right panel*)

the antenna beam. The mean values for the radar's beam tilt are accurate to within a few tenths of a degree under dynamic sea conditions.

In assessing the dynamic performance of the stabilizer, the ship's pitch, fore and aft, was typically far less active than the roll from side to side. The roll amplitudes normally varied up to near 5° while the pitch amplitudes varied about 2°. The period of the rolls was typically 10 s or less. The pitch and roll of the stabilized radar platform show a significant reduction in the standard deviation of the motion by a factor of about 10 for roll and about 5 for pitch during hourly measurements. These values were typical for most of the cruise. The radar operated at full sensitivity during leg 2 of VOCALS, days 316–337. A review of the time series of pitch and roll revealed short intervals when mean offsets and standard deviations were noisy and times when there were mean tilts that were larger than a few tenths of a degree. When sea conditions changed the gain values used to adjust the motion (K_p, K_i, K_d) were occasionally poorly matched to the new sea conditions and the beam pointing corrections were over-driven, causing the positioner to hit the mechanical stops and remain locked for short periods, sometimes an hour or more.

Figure 4 shows daily samples of the mean tilt and standard deviation of the radar beam compared to the ship's pitch and roll during the 22 days of leg 2. During the early part of this leg the control parameters were initialized and adjusted until the controller produced reliable operations. The first seven days showed that there were biases in the pointing that were corrected after the initial parameters were adjusted. After the early days the system's performance improved and the mean offsets and the fluctuations remained within favourable limits (mean offset ≈0.5°, standard deviation (STD) ≈0.3°). This provided a low-beam wander of less than a degree off vertical in both axes. For the entire leg 2 of the cruise where the radar was operating with good sensitivity the stabilizer operated successfully 89% of the 500 or so hours.

4.2 Cloud Observations

Studies of marine stratocumulus clouds over sea and coastal waters have been carried out in the past primarily by aircraft equipped with cloud radars and in situ probes (Vali et al. 1998). Observations to define the turbulence structures are important as turbulence within the cloud plays a significant role in the evolution of continental as well as marine stratus
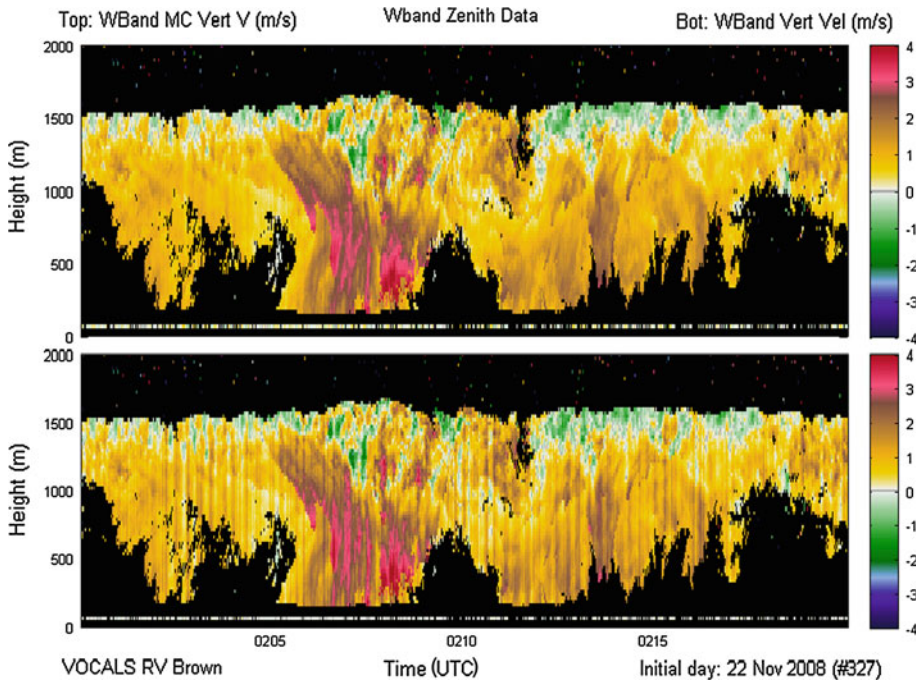
Fig. 5 Stabilized W-band radar velocity field: corrected for vertical ship motion (*upper panel*), without correction for ship motion (*lower panel*)

(Kollias and Albrecht 2000). Obtaining accurate measurements of the vertical structure of particle velocities leads to an understanding of the turbulence processes. The measurements pose a problem for aircraft observations as the platform motion must be removed from the velocity fields (Leon and Vali 1998). The use of millimetre-wavelength cloud radars aboard ship poses a similar set of problems as the motion of the ship has large amplitudes that significantly influence the measured cloud-particle velocity structure and maintaining stability of the radar is a challenge under varying sea conditions.

Information about cloud dynamics is derived from the Doppler spectrum of cloud particle motions. The radar provides estimates of the first three moments of the Doppler spectrum for each of the range volume samples: signal power or reflectivity (zeroth), vertical velocity (first) and spectral width (second). The full FFT spectrum for each sample is recorded on an external disc, producing about 1 Gigabyte of spectral data each hour. Height coverage for the VOCALS cruise is from about 200 m to 3 km with range resolution of 25 m and sampling times of 0.3 s (Table 1). The first gate is about 100 m higher than normal due to a minimum delay guard band installed as part of the repair in Arica.

The first step in processing the raw cloud measurements is to remove the effects of the ship's heave. Figure 5 shows a time-height display of the profile of radar vertical velocities for a 20-min set of measurements. The lower panel shows the raw profiles where vertical striping occurs due to the ships heave and the upper panel shows the velocity profiles corrected for the ship's motion. The vertical velocity of the ship, and hence radar platform, is measured by the Kongsberg sensor that is kept vertical by the stabilizer. The ship's motion is measured at a 10 Hz rate and the velocities are interpolated to the radar profiles that occur at a 3 Hz rate. Slight beam tilt on the order of 1° will cause very small errors (0.02%) in the applied
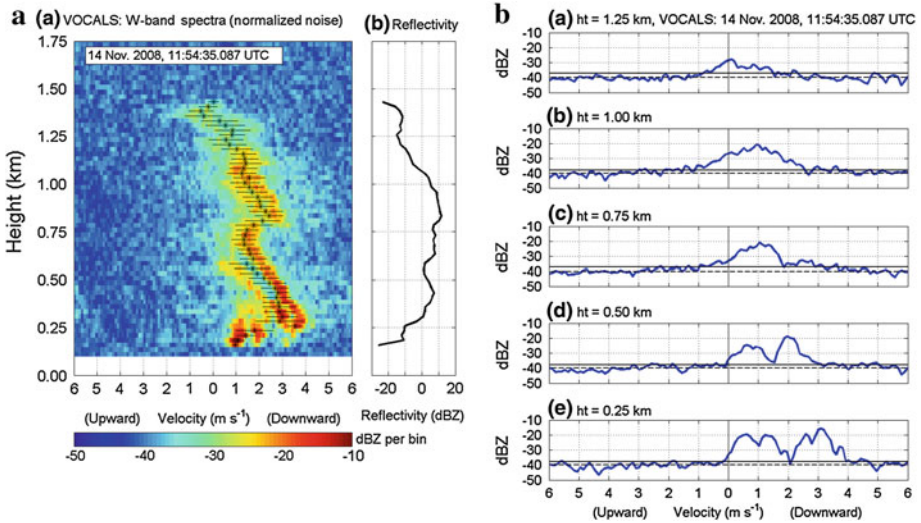
Fig. 6 a *Color* coded reflectivity contours of the normalized noise Doppler velocity spectra from a drizzle cloud during VOCALS 2008. *Asterisks* mark the mean velocity and short *horizontal lines* indicate spectral width. Range spacing is 25 m and dwell time is 0.3 s. **b** Doppler velocity spectra for five ranges separated by 250 m for the same cloud as in Fig. 6a. The development of separate droplet velocity distributions can be traced as the cloud particles descend

correction from the ship's heave. However, larger errors (on the order of 2%) can arise from strong horizontal winds inducing errors in the radial velocities of a tilted beam. Larger tilts will increase these effects. The corrected velocities may still contain some small effects of the horizontal wind induced errors.

A detailed example of spectra from a drizzle cloud is shown in Fig. 6a and shows a Doppler velocity power spectra profile during the VOCALS cruise at 14 November 2008, 1154:35.087 UTC. The right panel shows the reflectivity at each range gate (with 25-m resolution) and the left panel shows the reflectivity in each velocity bin using pseudo-colours. The spectra shown in Fig. 6a have been normalized so that the mean noise is constant with range to show the relative shape of the spectra with altitude. There are multiple peaks in the reflectivity spectra profile with 2–5 separate peaks observed below 0.5 km. Depending on the application, a single-peak can be defined as a continuous region of signal above the noise floor or multiple peaks can be defined as regions of signal between local minima (Shupe et al. 2004, 2008). Identifying multiple peaks allows for separating cloud properties based on spectral shape information (Rambukkange et al. 2011). Figure 6a shows the moments estimated from a single-peak picking method. The disagreement in mean velocity and spectral width when compared with the pseudo-colour peaks indicates that a multiple peak picking method could be applied to the spectra to investigate droplet distributions.

Figure 6b shows five Doppler velocity reflectivity spectra observed from 0.25 to 1.25 km in 250-m increments. The reflectivity spectra are normalized so that the mean noise is −40 dBZ (shown with a dashed line) and the maximum noise for each spectrum is shown with the solid black line. Two dominant peaks are observed in the spectra at 0.25-km and 0.50-km heights with minor peaks resolved at the lower height. These two dominant peaks could represent two distributions of scatterers with different cross-sections and fall speeds. The minor peaks are not instrumental artifacts because they evolve with time and height (images not shown).
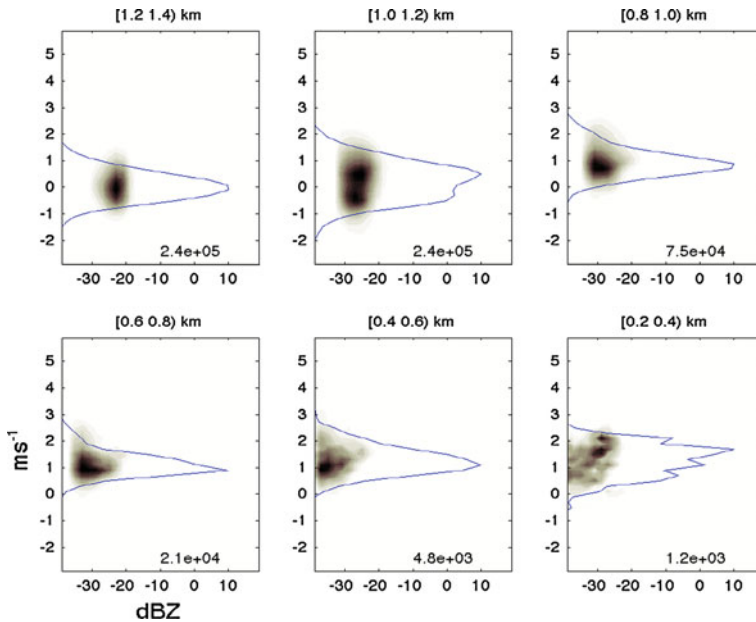
Fig. 7 Joint distribution of Doppler velocity and reflectivity within 200-m height intervals in a weakly drizzling stratocumulus cloud on 2008 November 18, 0400–0800 UTC (VOCALS). Positive velocities are downward (toward the radar antenna). The total number of observations above the noise for each level in the 4-hour period is indicated at the lower right of each panel

Note that instrumental artifacts would generate false signals at multiple harmonics of the real Doppler velocity or mirrored about zero velocity due to nonorthogonal I and Q voltages. A question to ask is: are the minimum reflectivities between the two peaks due to a continuous droplet distribution being observed with an oscillatory Mie backscattering function? If they are, then the minimum in reflectivity corresponds to backscattering from raindrops with approximately 1.65-mm diameter (Lhermitte 2002). Since raindrops with 1.65-mm diameter have a surface terminal fall speed of nearly $6 \, \text{m s}^{-1}$ and the minimum reflectivities occur in the spectra near $2 \, \text{m s}^{-1}$ downward velocities, then these droplet spectra at 0.25 and 0.50 km would need to be in an updraft of nearly $4 \, \text{m s}^{-1}$. Also, if there is only one continuous droplet distribution the first two maxima in the Mie backscattering occur approximately $2.75 \, \text{m s}^{-1}$ apart at about 4.5 and $7.25 \, \text{m s}^{-1}$. But the observed peaks are only about $2 \, \text{m s}^{-1}$ apart. Since it is unlikely that these spectra are in a $4 \, \text{m s}^{-1}$ updraft, and the separation between the peaks does not correspond with velocity spacing between the first two Mie backscattering maxima these multiple peak spectra are not due to variations in the Mie backscattering function, but are due to multiple rain droplet size distributions falling with different fall speeds.

Doppler velocity observations constrain cloud particle size and velocity distributions, from which microphysical processes can be inferred at different levels in the cloud. The Doppler velocity is the reflectivity-weighted sum of cloud droplets that move with the air velocity and drizzle drops, whose velocity is dominated by their fall speed. Cloud liquid water is greatest and cloud drops are largest at cloud top, while precipitation particles grow by collision-coalescence as they fall through the cloud.

Figure 7 shows joint Doppler velocity reflectivity distributions for six 200-m thick layers within and below a cloud sampled on 2008 November 18, 0400–0800 UTC during VOCALS.

Fig. 8 Combined profile of lidar and radar variance estimates from the surface to cloud base (lidar) and throughout the cloud (radar). The *black line* is an estimate of cloud base from a ceilometer
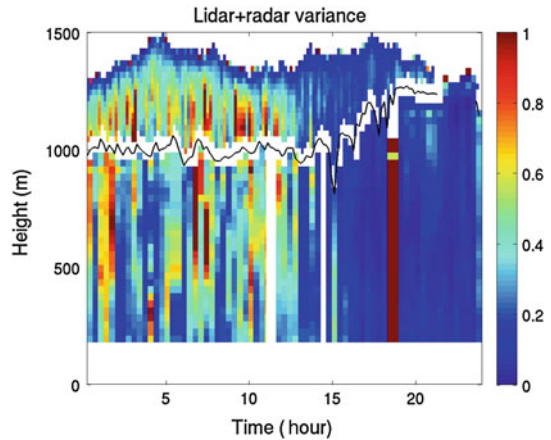
Near cloud top, from 1.2 to 1.4 km, particle velocities are distributed about zero indicating the radar measurements are not biased upward or downward. The distribution indicates a fairly uniform particle size as the reflectivity values are clustered near -20 dBZ. In the next lower 200 m level a bimodal velocity distribution develops with an increasing population of drizzle particles with positive fall speeds. More than 400 m below cloud top, the velocity distribution has a narrow downward peak centered at $\approx 1\,\mathrm{m\,s^{-1}}$, dominated by fall velocities of the drizzle drops. Though clouds and drizzle particles are probably both present, the larger more reflective drizzle particles dominate the Doppler velocity. Fewer meteorological reflectivities are observed below cloud base, showing drizzle decreases with distance below cloud base. The number of reflectivities above the noise is more than 200 times larger at cloud top (1.2–1.4 km) than at 0.2–0.4 km. The broad distribution of velocities (0–2.5 m s^{-1}) observed at 0.2–0.4 km indicates drizzle reaching the surface for about 0.5 % of the four hours during which the joint histogram was sampled.

During the VOCALS cruise the radar was co-located with a lidar (Tucker et al. 2009) that measured the characteristics of the aerosol particles in the column above the radar. While the radar can observe particles continuously through the cloud the lidar signal is often extinguished near cloud base. In this sense the two systems complement each other in providing a continuous measurement of the atmospheric turbulent velocity statistics. The time series of vertical velocity at a given altitude can be processed (Fang et al. 2011) to compute the variance, skewness, or turbulent kinetic energy dissipation rate. These can be used to compile complete boundary-layer time–height cross-sections. An example for velocity variance from VOCALS is shown in Fig. 8. The lidar provides the sub-cloud statistics and the radar the in-cloud statistics. This example shows intense vertical velocity variance during the night when longwave radiative cooling drives fairly intense turbulence throughout the boundary layer. During the day, solar heating (weighted near cloud top) tends to cancel the longwave cooling and the only remaining turbulence generation is principally surface wind shear. The skewness profiles (not shown) clearly indicate top-down convection during the night, which is consistent with cooling at cloud top.

5 Future Work

The need for minimizing the selection of the control parameters for the stabilizer is a goal for future cruises. At present, parameters are selected based on past experience with the system

and a preferred method would be based on an adaptive technique. The technique requires a more complex control algorithm and a new effort will be needed to modify the current system to upgrade to autonomous operation.

In addition to surface-based observations of marine clouds, another application for NOAA's transportable W-band radar is for airborne observations of sea spray-profiles of droplet distribution with height. This information is relevant to modelling the development of hurricanes. Small water droplets that are generated by winds and waves are carried aloft during storms and observing them with a nadir pointing W-band radar from an aircraft at 2 km altitude can be achieved if the radar's sensitivity is on the order of –20 dBZ. ESRL's Physical Science Division plans to operate the W-band radar in one of NOAA's P3 research aircraft. These aircraft make routine missions into storms at sea as part of NOAA's hurricane research programs. Radars operating at W-band have been used routinely for aircraft observations of clouds because of their favourable size, weight and high sensitivity to small water droplets (Pazmany et al. 1994; Li et al. 2004). Observations of storm generated sea spray from a surface platform are difficult due to the potential hazards and research programs designed to make those measurements have rarely been undertaken.

Airborne observations of sea spray using a nadir looking W-band radar have a much greater potential for success in making near-surface observations. Measurements of the profile of particle-drop size distribution would take place during a flight path that passed through the alternating bands of precipitating and clear regions in hurricanes. The clear regions will allow the radar to measure the return from sea spray without observing a mixture of sea spray and precipitation. The proposed operating characteristics for the radar configured for use on the P3 aircraft is shown in Table 1—column 3 along with a plot of the calculated sensitivity with height, Fig. 2.

A sea-spray source function (Fairall et al. 2009) is used to compute height profiles of drop size concentrations of sea-spray droplets as a function of wind speed. The measured backscattered reflectivity profiles are coupled with the drop size distribution estimates in a manner similar to Esteban-Fernandez et al. (2010). Larger particles have relatively high concentrations near the surface that decrease with altitude. With a nadir-pointing airborne radar, sensitivity to small droplets increases with altitude that coincides with the detection requirements in the model. Reflections from the sea surface may affect measurements up to 100 m making accurate estimates at or near the surface difficult. At an altitude of 2 km the sensitivity near the ocean surface is about –33 dBZ with the radar operating using 18-m range gates and short interval times between beams of 0.2 s.

The NOAA P3 aircraft have an unpressurized aft bay that is suitable to house the radar. A project is underway to repackage the radar's electronics in a pressure containment vessel to provide a suitable operating environment.

6 Summary

NOAA's Physical Science Division has fielded a new motion-stabilized W-band radar suitable for use aboard a ship for the study of marine boundary-layer clouds. With 25-m range gates and a 0.3-s dwell time, the sensitivity of the radar at 2 km is -33 dBZ, which provides detailed structure of the non-precipitating and weakly precipitating clouds over regions of the ocean where studies of air-sea interaction are important in modelling radiatively significant processes. The radar uses a servo controlled two-axis stabilizer to maintain the beam in the vertical and an integral velocity sensor to record vertical ship motion for post processing the velocity profiles to remove the effects of the ship's motion. Field tests during the VOCALS

2008 program demonstrate the effectiveness of the stabilization and the quality of the cloud measurements made using this new technique. Further applications of the new radar to the study of sea spray from an aircraft platform are underway and the radar's mechanical assembly is being engineered to fit the aft bay of a NOAA research aircraft for future flights in storms.

Appendix A: Radar and Calibration Details

Radar

The radar electronics for the shipboard radar is separated into the RF section at 94.56 GHz and the IF sections at 2,160 and 60 MHz (see the detailed radar block diagram, Fig. 9). The RF electronics include: (1) up converter from 2,160 MHz to 94.56 GHz, (2) transmitter driver circuits, (3) extended interaction klystron (EIK) amplifier, (4) high voltage power supply and modulator, (5) output detection and protection circuits, (6) antenna, (7) waveguide switches (circulators) used for receiver protection, (8) LNAs and calibration noise source, and (9) down converter to 2,160 MHz. All of the RF electronics are mounted in a tubular frame supported by the cradle in the beam stabilizer, Fig. 1. The stabilized platform and the radar electronics work independently.

Lapxm software from Vaisala provides modulation control of the transmit pulse and sampling control of the receiver. A digital IF receiver samples the return signal at 60 MHz and performs digital down conversion and filtering to the baseband frequency. GPS clock synchronization hardware maintains the data archive system clocks on the PCs to better than
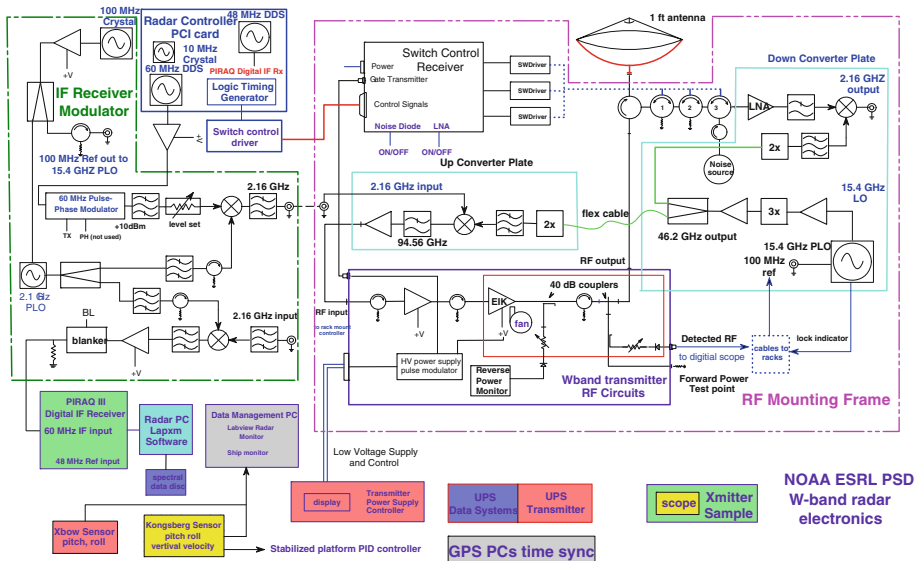
Fig. 9 W-band radar block diagram—RF mounting frame and rack mount electronics

0.1-s accuracy. A radar monitor software package archives the radar status along with the calibrated transmitted power.

The antenna (Cassegrain design) has about 46 dB gain with 0.7° beamwidth and sidelobes −18 dB below the main beam. The roof of the sea container that houses the radar has 1-m diameter cylinder with a rolled edge that acts as a shroud with a slanted dome cover. The cover is made of shrink wrap material and provides a low loss window (≈0.2 dB) through which the radar beam passes. A LNA with 5 dB noise figure is used in the receiver and provides a sensitivity of −120 dBm for 25-m range resolution operation. A fixed bias three-port circulator acts as a duplexer to isolate the transmitter and received signals by 25 dB. The receiver protection switches (circulators) provide 25–30 dB of isolation at each stage in the receiver chain providing an additional 90 dB of protection during the transmitted pulse sequence. The digital IF receiver uses 14 bits of sampled signal resolution and the digital down conversion hardware provides baseband signals for Doppler processing. A special software module was developed for the radar processor that provides calibrated reflectivity and produces netCDF output files.

The received power as measured by the digital receiver is extremely linear, better that 0.1 dB, for the range of signals up until saturation begins at about −41 dBm. The weakest detectable signals are better than −115 dBm and provide a linear dynamic range over 70 dB. A received narrow band signal with a level of −55 dBm would correspond to an echo from a +27 dBZ cloud at 2 km. This level is near the upper limit for W-band scattering measurements in the non-Raleigh region, typically in the range of 25–30 dBZ.

Calibration

Radar calibration usually takes two forms: an internal calibration of individual system components or an external calibration using a target with known radar cross-section. The internal method is sometimes easier to achieve, however the additive error from each individual calibration can create a larger than desired overall calibration uncertainty. As we had access to reasonably good test equipment and reliable antenna pattern measurements of gain and beamwidth we were able to use the internal method for the initial radar calibration.

To provide accurate estimates of reflectivity as expressed in Eq. 1, the radar's calibration requires, (1) individual calibrations of the system's components that make up the computation of the radar constant in Eq. 2, including the peak transmitted power, (2) an accurate estimate of the distance to each range cell, and (3) a calibration of the received power at the output of the antenna. The individual component's measurements can be carried out with laboratory test equipment and the range calibration is performed with a delay line. The transmitted power is measured hourly and the reflectivity computations use the most up-to-date value.

Calibration of the radar's receiver is important in order to obtain a measure of the received power at the antenna terminals prior to entering the LNA. The processed signal gain, G_{RP}, is used to convert the power estimated by the processor, in units of analog-to-digital converter (ADC) counts, into calibrated received power, in milliwatts. We have chosen the processed signal gain (G_{RP}) to be the ratio of the power measured by the processor (P_{RP}) to the receiver power at the antenna terminals (P), in milliwatts,

$$G_{RP} = \frac{P_{RP}}{P}. \tag{6a}$$

Changing to units of dB and rearranging

$$P = P_{RP} - G_{RP} \tag{6b}$$

where P is the received power in decibels above a milliwatt (dBm) at the output terminals of the antenna equivalent to the power at the input to the LNA, assuming a good electrical match at the interface. We use a noise diode with known excess noise ratio (ENR) and inject this into the LNA at the front end of the RF down converter stages (Fig. 9). The output noise power of the diode, N_D, can be computed from the ENR. The gain will be the difference, in dB, between the measured noise added by the diode and the calibrated diode noise power:

$$G_{RP} = N_{RP} - N_D \tag{7}$$

where N_{RP} is the total added noise with the diode on, measured by the radar's processor. The signal processing software estimates the mean noise power in the spectrum using the method of Hildebrand and Sekhon (1974). The technique to measure the added noise uses the standard Y factor computation that relies on two measurements of the spectral noise, one with the diode on and one with it off. The measured noise added by the diode is

$$N_{RP} = (\langle N_{diodeON} \rangle - \langle N_{diodeOFF} \rangle) \, N_P \tag{8a}$$

or expressed in units of dB

$$N_{RP}(dB) = 10 \log_{10}(N_{RP}) \tag{8b}$$

where $\langle N_{diodeON} \rangle$ and $\langle N_{diodeOFF} \rangle$ are the linear mean noise powers per FFT point with the diode on and off, respectively and N_P is the number of points in the FFT.

Using a receiver with a noise equivalent bandwidth, B_{NE}, the noise power from the diode with noise temperature T_D is

$$N_D = 10 \log_{10}(k \, T_D \, B_{NE}). \tag{9}$$

The temperature of the diode is

$$T_D = L T_0 \left(10^{\frac{ENR_{dB}}{10}} + 1 \right) + (1 - L) \, T_0 \tag{10}$$

where T_0 is the ambient room temperature, L is any loss between the diode and the LNA and ENR_{dB} is the diode's excess noise ratio in dB.

Using this method we computed the gain through the receiver and radar processor to be 185.2 dB (Table 2). (This is an artificially high value due to internal scale factors used in the software that computes the spectral power.) We estimated the possible errors in each of the component's calibration, including antenna gain and beamwidths, waveguide losses and calibration of the noise source with a resultant uncertainty of 2 dB. This is usually an acceptable range for errors in the estimate of radar reflectivity. Future plans call for a field calibration of the radar using a target with known radar cross-section. This is a preferred method as it reduces the number of component calibrations; however it still has a drawback since it must rely on atmospheric conditions that are favourable for the tests.

Appendix B: Using Doppler Power Spectrum Statistics to Estimate a Minimum Detectable Signal to Noise Threshold

This appendix describes how the signal and noise statistics of a Doppler velocity power spectrum are used to estimate a minimum detectable signal useful for estimating the radar's minimum detectable reflectivity. The NOAA W-band radar uses the profiler signal processing method described in Carter et al. (1995) to collect and estimate the Doppler velocity power

spectrum. The observed spectrum contains both signal and noise at each frequency bin. At a particular frequency f_i, with Doppler frequency resolution Δf, spectral noise density is

$$n(f_i) = \langle n \rangle \pm \sigma_{noise} \tag{11}$$

where $\langle n \rangle$ is the mean noise density and σ_{noise} is the standard deviation of the noise density. The noise density standard deviation decreases with averaging more spectra such that

$$\sigma_{noise} = \frac{\langle n \rangle}{\sqrt{N_F}} \tag{12}$$

where N_F is the number of FFTs averaged to form the observed power spectrum. Since the Doppler power spectral density, S, contains both signal and noise power densities, the total signal and noise powers are summations over the spectrum given by

$$Signal = S_S = \sum_{i=1}^{i=N_P} (S(f_i) - n(f_i)) \Delta f = \sum_{i=1}^{i=N_P} (S(f_i) - \langle n \rangle) \Delta f \tag{13}$$

$$Noise = N_S = \sum_{i=1}^{i=N_P} n(f_i) \Delta f = \sum_{i=1}^{i=N_P} \langle n \rangle \Delta f = \langle n \rangle \Delta f N_P \tag{14}$$

where N_P is the number of points in the FFT spectrum.

For a weak signal confined to one frequency bin to be detected it should be greater than the standard deviation of the spectral noise (σ_{noise}) by some value a or

$$S_S = (S - \langle n \rangle) > a\sigma_{noise} \tag{15}$$

where a, the threshold factor, is defined by the probability function

$$PROB \ (S_S > a\sigma_{noise}) \, N_P \cong 1. \tag{16}$$

This condition follows from the requirement that we only expect no more than one out of N_P to exceed $\langle n \rangle$ by $a\sigma_{noise}$.

If we assume a Gaussian shape to the signal-to-noise distribution, we can use a form of the error function, *erfc*, to estimate the probability that the signal exceeds $\langle n \rangle$ by $a\sigma_{noise}$:

$$PROB\,(X > \kappa\sigma) = Q\,(\kappa), \tag{17a}$$

$$Q\,(\kappa) = \frac{1}{2} erfc \, \frac{\kappa}{\sqrt{2}}. \tag{17b}$$

From Eq. 17 we can compute the expected values of a for several FFTs.
For $N_P = 128 PROB\,(S_S > a\sigma_{noise}) = 7.81 \times 10^{-3} = Q\,(a) \quad \Rightarrow a \approx 2.45.$
For $N_P = 256 \ PROB\,(S_S > a\sigma_{noise}) = 3.91 \times 10^{-3} = Q\,(a) \quad \Rightarrow a \approx 2.68.$
Now

$$Signal = S_S = a\sigma_{noise}\Delta f, \tag{18}$$

and combining with Eqs. 12 and 14 we have the minimum signal-to-noise ratio threshold

$$\frac{Signal}{Noise} = \frac{S_S}{N_S} = \frac{a\sigma_{noise}\Delta f}{\langle n \rangle \, \Delta f N_P} = \frac{a}{N_P \sqrt{N_F}} \tag{19}$$

Thus, we can estimate the expected minimum signal-to-noise ratio threshold for detecting a cloud boundary in terms of variables in (19) as $SNR_{min} = 10 \log_{10} \frac{Signal}{Noise}$.
For $N_P = 128$, $N_F = 8$ and $a = 2.45$, $SNR_{\mathbf{min}} = -21.7 \, dB$.
For $N_P = 256$, $N_F = 8$ and $a = 2.68$, $SNR_{\mathbf{min}} = -24.3 \, dB$.

References

Ackerman TP, Stokes G (2003) The atmospheric radiation measurement program. Phys Today 56:38–45

Benedict RR (1967) Electronics for scientists and engineers. Prentice Hall, Englewood Cliffs, 635 pp

Bretherton CS, Uttal T, Fairall CW, Yuter SE, Weller RA, Baumgardner D, Comstock K, Wood R (2004) The EPIC 2001 Stratocumulus Study. Bull Am Meterol Soc 85:967–977

Carter DA, Gage KS, Ecklund WL, Angevine WM, Johnston PE, Riddle AC, Wilson J, Williams CR (1995) Developments in UHF lower tropospheric wind profiling at NOAA's Aeronomy Laboratory. Radio Science 30:977–1002

Damiani R, Vali G, Haimov S (2006) The structure of thermals in cumulus from airborne dual-Doppler radar observations. J Atmos Sci 63:1432–1450

Dong X, Minnis P, Xi B (2005) A climatology of midlatitude continental clouds from the ARM SGP central facility. Part I: Low-level cloud macrophysical, microphysical, and radiative properties. J Clim 18:1391–1410

Doviak RJ, Zrnic DS (1993) Doppler radar and weather observations. Academic Press, New York, 562 pp

Esteban-Fernandez D, Durden SL, Chaubell J, Cooper KB (2010) Design considerations for a dual-frequency radar for sea spray measurement in hurricanes. In: Geoscience and Remote Sensing Symposium (IGARSS), 2010 IEEE International, pp 2896–2899, 25–30 July 2010. doi:10.1109/IGARSS.2010.5653198

Fairall CW, Banner ML, Peirson WL, Morison RP, Asher W (2009) Investigation of the physical scaling of sea spray spume droplet production. J Geophys Res 114:C10001. doi:10.1029/2008JC004918

Fairall CW, Moran K, Pezoa S, Wolfe DE, de Szoeke S, Ghate V (2010) A new motion-stabilized W-band (94-GHz) cloud radar for observations of marine boundary-layer clouds. Preprints of the ISARS symposium, Paris, France, 28–30 June 2010. http://www.isars2010.uvsq.fr; Paper O-MEA/01

Fang M, Albrecht BA, Kollias P, Ghate VP (2011) Turbulence estimates in continental stratocumulus using ARM Cloud Radar Data. DOE ASR/ARM Annual Science Team Meeting, San Antonio, TX. http://asr.science.energy.gov/meetings/stm/posters/poster_pdf/2011/P000372.pdf

Frisch AS, Fairall CW, Snider JB (1995) Measurement of stratus cloud and drizzle parameters in ASTEX with a Ka-band Doppler radar and microwave radiometer. J Atmos Sci 52:788–799

Gossard EE (1988) Measuring drop size distributions in cloud with a clear-air sensing Doppler radar. J Atmos Ocean Technol 5:640–649

Gossard EE (1994) Measurements of cloud droplet size spectra by Doppler radar. J Atmos Ocean Technol 11:712–726

Hildebrand PH, Sekhon RS (1974) Objective determination of the noise level in Doppler spectra. J Appl Meteorol 13:808–811

Kollias P, Albrecht BA (2000) The turbulent structure in a continental stratocumulus cloud from millimeter wavelength radar observations. J Atmos Sci 57:2974–2992

Kollias P, Fairall CW, Zuidema P, Tomlinson J, Wick GA (2004) Observations of marine stratocumulus in SE Pacific during the PACS 2003 cruise. Geophys Res Lett 31:L22110. doi:10.1029/2004GL020751

Kollias P, Clothiaux EE, Miller MA, Albrecht BA, Stephens GL, Ackerman TP (2007) Millimeter-wavelength radars—new frontier in atmospheric cloud and precipitation research. Bull Am Metereol Soc 88:1608–1624

Leon D, Vali G (1998) Retrieval of three-dimensional particle velocity from airborne Doppler radar data. J Atmos Ocean Technol 15:860–870

Lhermitte RM (1987) A 94-GHz Doppler radar for cloud observations. J Atmos Ocean Technol 4:36–48

Lhermitte RM (1988) Observations of rain at vertical incidence with a 94 GHz Doppler radar: an insight of Mie scattering. Geophys Res Lett 15:1125–1128

Lhermitte RM (1990) Attenuation and scattering of millimeter wavelength radiation by clouds and precipitation. J Atmos Ocean. Technol 7:464–479

Lhermitte RM (2002) Centimeter and millimeter wavelength radars in meteorology. Lhermitte Publications, Miami, 550 pp

Li L, Heymsfield GM, Racette PE, Tian L, Zenker E (2004) A 94-GHz cloud radar system on a NASA high-altitude ER-2 aircraft. J Atmos Ocean Technol 21:1378–1388

Mace GG, Heymsfield AJ, Poellot MR (2002) On retrieving the microphysical properties of cirrus clouds using the moments of the millimeter wavelength Doppler spectrum. J Geophys Res 107:4815. doi:10.1029/2001JD001308

Moran KP, Martner BE, Post MJ, Kropfli RA, Welsh DC, Widener KB (1998) An unattended cloud-profiling radar for use in climate research. Bull Am Meteorol Soc 79:443–445

Pazmany AL, McIntosh RE, Kelly R, Vali G (1994) An airborne 95-GHz dual polarization radar for cloud studies. IEEE Trans Geosci Remote Sens 1:731–739

Probert-Jones JR (1962) The radar equation in meteorology. Q J Roy Meteorol Soc 88:485–495

Rambukkange MP, Verlinde J, Eloranta EW, Flynn CJ, Clothiaux EE (2011) Using Doppler spectra to separate hydrometeor populations and analyze ice precipitation in multilayered mixed-phase clouds. IEEE Geosci Remote Sens Lett 8:108–112

Riddle AC, Gage KS, Balsley BB, Ecklund WL, Carter DA (1989) Poker Flat MST Radar Data Bases. NOAA Tech., Memorandum, ERL AL-11

Sekelsky SM, McIntosh RE (1996) Cloud observations with polarimetric 33 GHz and 95 GHz radar. Meteorol Atmos Phys 59:123–140

Sekelsky SM, Ecklund WL, Firda JM, Gage KS, McIntosh RE (1999) Particle size estimation in ice-phase clouds using multi-frequency radar reflectivity at 95, 33, and 2.8 GHz. J Appl Meteorol 38:5–28

Shupe MD, Kollias P, Matrosov SY, Schneider TL (2004) Deriving mixed-phase cloud properties from Doppler radar spectra. J Atmos Ocean Technol 21:660–670

Shupe MD, Daniel JS, de Boer G, Eloranta EW, Kollias P, Long CN, Luke EP, Turner DD, Verlinde J (2008) A focus on mixed-phase clouds. Bull Am Meteorol Soc 89:1549–1562

Stephens GL, Tsay SC, Stackhouse PW, Flatau PJ (1990) The relevance of the microphysical and radiative properties of cirrus clouds to climate and climate feedback. J Atmos Sci 47:1742–1752

Tucker SC, Brewer WA, Banta RM, Senff CJ, Sandberg SP, Law DC, Weickmann AM, Hardesty RM (2009) Doppler lidar estimation of mixing height using turbulence, shear, and aerosol profiles. J Atmos Ocean Technol 26(4):673–688

Vali G, Kelly R, Pazmany A, McIntosh RE (1995) Airborne radar and in-situ observations of a shallow stratus with drizzle. J Atmos Res 38:361–380

Vali G, Kelly R, French J, Haimov S, Leo D, McIntosh R, Pazmany A (1998) Fine-scale structure and microphysics of coastal stratus. J Atmos Sci 55:3540–3564

Webster PJ, Fairall CW, Hacker PW, Lukas R, Bradley EF, Godfrey S (2002) The Joint Air-Sea Monsoon Interaction Experiment (JASMINE) Pilot study. Bull Am Meteorol Soc 83:1603–1630

Woods R, 32 coauthors, (2011) The VAMOS Ocean-Cloud-Atmosphere-Land Study Regional Experiment (VOCALS-REx): goals, platforms, and field operations. Atmos Phys Chem Discuss 11:2627–654. doi:10.5194/acp-11-627-2011